Rüdiger Quay

SPRINGER SERIES IN MATERIALS SCIENCE 96

Gallium Nitride Electronics

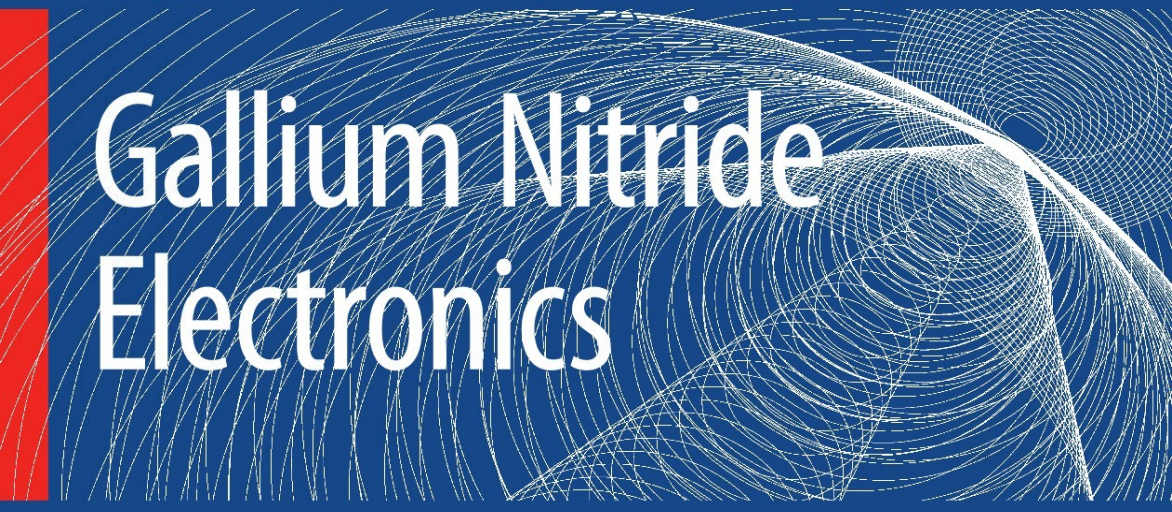

Springer

Springer Series in
MATERIALS SCIENCE 96

Springer Series in

MATERIALS SCIENCE

Editors: R. Hull R. M. Osgood, Jr. J. Parisi H. Warlimont

The Springer Series in Materials Science covers the complete spectrum of materials physics, including fundamental principles, physical properties, materials theory and design. Recognizing the increasing importance of materials science in future device technologies, the book titles in this series reflect the state-of-the-art in understanding and controlling the structure and properties of all important classes of materials.

99 **Self-Organized Morphology in Nanostructured Materials**
Editors: K. Al-Shamery and J. Parisi

100 **Self Healing Materials**
An Alternative Approach to 20 Centuries of Materials Science
Editor: S. van der Zwaag

101 **New Organic Nanostructures for Next Generation Devices**
Editors: K. Al-Shamery, H.-G. Rubahn, and H. Sitter

102 **Photonic Crystal Fibers**
Properties and Applications
By F. Poli, A. Cucinotta, and S. Selleri

103 **Polarons in Advanced Materials**
Editor: A.S. Alexandrov

104 **Transparent Conductive Zinc Oxide**
Basics and Applications in Thin Film Solar Cells
Editors: K. Ellmer, A. Klein, and B. Rech

105 **Dilute III-V Nitride Semiconductors and Material Systems**
Physics and Technology
Editor: A. Erol

106 **Into The Nano Era**
Moore's Law Beyond Planar Silicon CMOS
Editor: H.R. Huff

107 **Organic Semiconductors in Sensor Applications**
Editors: D.A. Bernards, R.M. Ownes, and G.G. Malliaras

108 **Evolution of Thin-Film Morphology**
Modeling and Simulations
By M. Pelliccione and T.-M. Lu

109 **Reactive Sputter Deposition**
Editors: D. Depla amd S. Mahieu

110 **The Physics of Organic Superconductors and Conductors**
Editor: A. Lebed

Volumes 50–98 are listed at the end of the book.

Rüdiger Quay

Gallium Nitride Electronics

Springer

Dr. Rüdiger Quay
Fraunhofer Institut für Angewandte Festkörperphysik (IAF)
Tullastr. 72, 79108, Freiburg, Germany

Series Editors:

ISBN 978-3-540-71890-1 e-ISBN 978-3-540-71892-5

DOI 10.1007/978-3-540-71892-5

Springer Series in Materials Sciences ISSN 0933-033X

Library of Congress Control Number: 2008924620

Typesetting and production: le-tex publishing services oHG, Leipzig, Germany
Cover design: WMXDesign, Heidelberg, Germany

Printed on acid-free paper

9 8 7 6 5 4 3 2 1

springer.com

To our son, Jonathan Benedikt

In memoriam, Oliver Winterer (1970–2006)

Preface

Electronic RF-communication and sensing systems have dramatically changed our daily lives since the invention of the first electronic transistor in 1947. Advanced semiconductor devices are key components within electronic systems and ultimately determine their performance. In this never ending challenge, wide-bandgap nitride semiconductors and heterostructure devices are unique contenders for future leading-edge electronic systems due to their outstanding material properties with respect to speed, power, efficiency, linearity, and robustness. At the same time, their material properties are challenging compared with any other material system due to high growth temperatures and many other intrinsic properties.

Wide bandgap semiconductors have attracted a lot of attention in the last ten years due to their use in optoelectronic and electronic applications. The field is developing rapidly due to the high investments in US, Japanese, and increasing European research and development activities. Some of the knowledge acquired may not be available to the general public because of military or civil restrictions. However, this work compiles and systemizes the available knowledge and evaluates remaining issues. This book is of interest to graduate students of electrical engineering, communication engineering, and physics; to material, device, and circuit engineers in research and industry; and to scientists with general interest in advanced electronics.

The author specially thanks those people, without whom and without whose individual contributions such a challenging work would have been impossible. He owes special thanks to:

Prof. Dr. Günter Weimann, director of the Fraunhofer Institute of Applied Solid-State Physics (IAF), for his encouragement, his advice, and continuous support.

Prof. Dr. Joachim Wagner for the encouragement to start this project.

Prof. Dr. Siegfried Selberherr, Insitut für Mikroelektronik, TU Wien, for continuous encouragement and support.

Dr. Michael Schlechtweg, head of the RF-device and circuits department at Fraunhofer IAF, and *Dr. Michael Mikulla*, head of the technology department at Fraunhofer IAF, for their generous support.

Dr. Rudolf Kiefer for his outstanding contributions and careful advise on the technology chapter, for his kind understanding, and for valuable discussions.

Dipl.Phys. Stefan Müller and *Dr. Klaus Köhler* for their valuable contributions of the epitaxy chapter and for proof reading.

Dr. Friedbert van Raay for his proof reading, contributions to large-signal modeling and circuit design and for countless discussions on modeling, large-signal measurements, layout, and circuit design.

Dr. Michael Dammann, Dipl.Ing. Helmer Konstanzer, and *Andreas Michalov* for their contributions and their work on device reliability.

Dr. Wolfgang Bronner for his contributions to the development of technology and the SiC back-end process.

Dr. Wilfried Pletschen for his thorough proof reading and his kind advise on etching.

Dr. Matthias Seelmann-Eggebert for his inspired work on thermal simulations and large-signal modeling.

Dr. Patrick Waltereit for numerous fruitful discussions on epitaxial and process development.

Dipl.Ing. Daniel Krausse for his work on low-noise amplifiers.

Dr. Vassil Palankovski and *Dipl.Ing. Stanislav Vitanov*, TU Vienna, for proof reading and their valuable support on physical device simulation.

Dr. Axel Tessmann for his continuous good mood and valuable motivation for the development of mm-wave technology.

Markus Riesle and *Dr. Herbert Walcher* for their contributions to the MMIC module and device packaging.

Martin Zink and *Ronny Kolbe* for the patient dicing and picking of a numerous MMICs.

Dipl.Ing. Christoph Schwörer for valuable discussions on circuit design and for his contribution on the broadband amplifiers.

Dr. Lutz Kirste for his help on crystal structures.

Dipl.Ing. Michael Kuri , *Dipl.Ing. Hermann Massler* and the members of the RF-devices and circuits characterization group at Fraunhofer IAF for their support.

Dr. Arnulf Leuther for wise hints and good cooperation on process development.

Fouad Benkhelifa for his creative and careful development of processing technology and for active discussions.

Further, I would like to thank the technical staff in the Fraunhofer RF-devices-and-circuit and technology-departments, especially *Dr. Gundrun Kauffel* and *W. Fehrenbach.*

Dr. Hardy Sledzik, Dr. Patrick Schuh, Dr. Ralf Leberer, and *Dr. Martin Oppermann* at EADS DE in Ulm for good cooperation and for valuable discussions.

Dipl.Ing. Dirk Wiegner, Dr. Wolfgang Templ, and *Ulrich Seyfried* at the Research Center at Alcatel-Lucent/Stuttgart for outstanding cooperation on highly-linear power amplifiers.

Dr. Thomas Rödle and his team at NXP research center, Nimwegen, for good cooperation on power amplifier technology.

The Team at United Monolithic Semiconductors (UMS), Ulm for good cooperation on device technology.

Mark van Heijningen and *Dr. Frank van Vliet* at TNO Safety and Security, the Hague, Netherlands, for the good cooperation on high-power amplifiers at Ka-band.

Joyce Visne, Wien, for her patient and thorough language corrections and her kind support.

The Springer team, especially, *Adelheid Duhm* and *Dr. Claus Ascheron* for their great support and kind understanding.

The le-tex team, especially *Steffi Hohensee*, for their kind support.

I thank my wife Christine and my son Jonathan, to whom this book is dedicated, for their endless patience.

Freiburg i.Br. *Rüdiger Quay*
Januar 2008

Contents

List of Symbols

Δ	Step, difference, change
ΔE_{V}, ΔE_{C}	Discontinuity of the valence/conduction band at a heterointerface
ΔE_{g}	Total difference of the bandgaps at a heterointerface
Δf	Frequency interval
ΔV	Voltage drop over the depletion zone
$\Theta(T_0)$	Temperature-dependent thermal resistance
α, β, γ	General exponent
α	General temperature coefficient
α	Common base current gain
α_a, α_c	Coefficients of thermal expansion along a- and c-axis
α_{AB}	Temperature exponent of the ternary $\mathrm{A}_x\mathrm{B}_{1-x}$
α_{H}	Hooge parameter
α_n, α_p	Impact ionization parameter for electrons and holes
α_n	Fitting parameter in the LS-model
α_{T}	Base transmission factor
α_{S}	Fitting parameter in the LS-model
β	Common emitter current gain in bipolar devices
γ_{i}	Emitter injection efficiency
δ	The base recombination factor
ε	Permittivity
ϵ_{ij}	Dielectric tensor components
ϵ_0	Dielectric constant
ε_{r}	Relative permittivity

$\varepsilon_{\mathrm{r}}^{\mathrm{eff}}$	Effective permittivity
$\varepsilon_{\mathrm{r}}^{\mathrm{inf}}$	Relative permittivity for $\omega \to \infty$
η_{d}	Drain efficiency
κ_{L}	Lattice thermal conductivity
$\kappa_{\mathrm{L}}(T)$	Thermal conductivity as a function of temperature
$\kappa_{300}^{\mathrm{A}}$	Thermal conductivity at 300 K of material A
λ_{n}	Fitting parameter in the LS-model
μ_ν	Mobility of carrier type ν
μ_{AB}	Mobility of the ternary semiconductor $A_xB_{1-x}N$
τ	Phase term of the transconductance g_{m}
τ_{thermal}	Thermal time constant
ϕ_{B}	Schottky barrier potential
ψ	Electrostatic potential
ψ_i	Polynomials of the potential
ρ_{s}	Semiconductor resistivity
ρ_{c}	Metal resistivity
σ_{B}	Total interface charge at the boundary
$\sigma_{\mathrm{B,SP}}$	Interface charge due to spontaneous polarization
$\sigma_{\mathrm{B,PZ}}$	Interface charge due to piezoelectric polarization
σ_A	Electric drift-region-conductance per unit area in the semiconductor
τ_{D}	The delay due to the extension of the depletion zone to the drain
τ	Small-signal phase constant
τ_{RC}	Channel-charge RC-delay
τ_{T}	Total delay
$\tau_{\mathrm{e}}, \tau_{\mathrm{b}}, \tau_{\mathrm{c}}$	Emitter, base, collector delay
τ_{TR}	Transistor delay
τ_{thermal}	Thermal time constant
ω	Oscillation frequency
A	Area
A_{R}	Richardson constant
$A_1, \ldots, A_n$	General coefficient
A_ν	Coefficient for impact ionization for carrier ν = n,p
B	Direct radiative recombination parameter
B_0	Bulk modulus
BV_{CE0}	Open collector–emitter breakdown voltage

BV_{DS}	Drain–source breakdown voltage
$BV_{\mathrm{DS\ RF}}$	RF drain–source breakdown voltage
BV_{GD}	Gate–drain diode breakdown voltage
BV_{GS}	Gate–source diode breakdown voltage
C	Correlation parameter
C	Capacitance in the passive model
C_{ij}	Elastic constants index i, j
C_{th}	Thermal capacitance
C_{ds}	Drain–source capacitance
C_{g}	Gate capacitance
C_{gd}	Gate–drain capacitance
C_{gs}	Gate–source capacitance
C_{jc}	Collector junction capacitance
C_{je}	Emitter junction capacitance
C_{pds}, C_{pgs}, C_{pgd}	Parasitic drain–source, gate–source, and gate–drain capacitances
$C_{\mathrm{gs,0}}$,$C_{\mathrm{gd,0}}$	Large-signal charge modeling coefficients
C_0	Static capacitance
C_{ss}	Parasitic capacitance in the dispersion model
C_{th}	Thermal capacitance
D_{nB},D_{pE}	Diffusivity of electrons in the base, holes in the emitter
$\boldsymbol{E}$	Local electric field
E_{A}	Acceptor energy
E_{a}	Activation energy
E_{break}	Breakdown field
E_{crit}	Critical field
E_{C}	Conduction band energy
$E_{\mathrm{F}}(x)$	Fermi energy at position x
$\mathrm{E_{f1}}$	Fermi-level correction energy
E_{g}	Bandgap energy
$E_{\mathrm{g},\Gamma}$	Bandgap energy in the Γ-valley
$E_{\mathrm{g},\Gamma 1}$, $E_{\mathrm{g},\Gamma 3}$	Bandgap energy in the Γ_1, Γ_3-valley
$E_{\mathrm{g,G-A}}$	Bandgap energy in the G–A valley
$E_{\mathrm{g,L}}$	Bandgap energy in the L-valley
$E_{\mathrm{g,L-M}}$	Bandgap energy in the L–M valley
$E_{\mathrm{g,X}}$	Bandgap energy in the X-valley
$E_{\mathrm{g},0}$	Bandgap energy at $T_{\mathrm{L}}= 0\,\mathrm{K}$
E_{V}	Valence band energy
G	Conductance in the passive model
G_{ass}	Associated gain
G_{p}	Power gain
$G_{\mathrm{m},2}$, $G_{\mathrm{m,d}}$, $G_{\mathrm{m},2,\mathrm{d}}$	Current parameters in Volterra approach
H	Hardness

I_0	Current parameter in the diode equation
I_0	Current at time t= 0
I_B, I_C, I_E	Base, collector, and emitter currents
I_D	Drain current
I_Dmax,I_Dmin	Maximum, minimum drain current
$I_\mathrm{Dmax,RF}$, $I_\mathrm{Dmin,RF}$	Maximum/minimum RF-drain current
I_DS	Drain–source current
I_Dpp	Peak-to-peak drain current
I_Dsat	saturated drain current
I_DSn,I_DSp	Drain–source current in the LS-modeling
I_Dq	Quiescent drain current
I_DSS	Saturated drain current, typically at $V_\mathrm{GS} = 0\,\mathrm{V}$
I_G	Gate current
II_3	Ratio of input intermodulation 3rd order
IM_3	Intermodulation distortion ratio 3rd order
IMD_3	Intermodulation distortion 3rd order
I_{ij}	Current at port with index i,j
I_opt	Drain current optimized for noise figure
I_pk, I_pk0	Peak current parameter in LS-model
$\mathrm{K_{bg}}$	Dispersion parameter in the LS-model
$\mathrm{K_{trg}}$	Soft-breakdown pinch-off parameter
K_C	Fracture toughness
L	Channel length
L	Line inductance in the passive model
L_e	Emitter length
L_D, L_G, L_S	Drain, gate, and source inductances
L_D	Length of the depletion zone
L_sb	Soft breakdown function
L_sb0	LS-parameter for the soft-breakdown
L_sd1	Auxiliary function
MAG	Maximum available gain
M_C	Number of equivalent minima at the conduction band
MSG	Maximum stable gain
MTBF	Median time before failure
MTTF	Median time to failure
N_A	Acceptor doping concentration
N_B	Base carrier concetrations
N_C	Effective density of states of the conduction band
N_D	Donor doping concentration
$\mathrm{N_{DC}}$	Donor doping concentration in the collector

N_{E}	Emitter carrier concentration
N_{F}	Noise figure
$N_{\mathrm{F,min}}$	Minimum noise figure at optimum impedance
N_{T}	Concentration of traps
N_{V}	Effective density of states of the valence band
OIP_3	Output intercept point third order
P_i	Function in the charge model
PAE	Power-added-efficiency
$P_{-1\mathrm{dB}}$	Output power at 1 dB compression
P_{DC}	DC-power
P_{diss}	Dissipated power
P_{in}	Input power
P_{ij}	Large-signal parameter for the pinch-off voltage
P_{out}	Output power
P_{SP}	Spontaneous polarization
P_{PZ}	Piezoelectric polarization
P_{sat}	Saturated output power
R	Resistance
R_{Con}	Contact resistance
R_{D}	Drain resistance
$R_{\mathrm{D,semi}}$	Semiconductor contribution to R_{D}
R_{L}	Load resistance/impedance
$R_{\mathrm{S,met}}$, $R_{\mathrm{D,met}}$	Metal contribution to R_{S} and R_{D}
R_{S}, R_{G}, R_{D}	Parasitic source, gate, and drain resistances
R_{S}	Series resistance of diode
R_{band}	Band edge contribution to the source resistance R_{S}
R_{bb}	Base resistance
R_{chan}	Channel resistance
R_{ds}	Drain–source resistance
R_{gap}	Contribution of the contact gap to R_{bb}
R_{gd},R_{gs}	Gate–drain/–source resistance
R_{i}	Input resistance
R_{n}	Equivalent noise resistance
R_{on}	On-resistance
R_{opt}	Optimum impedance
R_{spread}	Spread contribution to R_{bb}
R_{ss}	Parasitic output resistance in the dispersion model
R_{th}	Thermal resistance
S_{ij}	Scattering (S-) parameter, $i, j = 1, 2$

$S_\nu(f)$	Spectral noise density
T_{chan}	Channel temperature
T_{Debye}	Debye-temperature
T_{Drain}, T_{Gate}	Drain and gate noise-temperature
$T(E_x)$	Tunneling probability
T_{L}	Local lattice temperature
T_{sub}	Substrate temperature
T_0	Backside temperature in the LS-model
U	Unilateral gain
V_1	Variable in the Curtice model
V_{BE}, V_{CE}, V_{BC}	Base–emitter, collector–emitter, and collector–base voltages
$V_{\mathrm{breakdown}}$	Breakdown voltage
V_{DS}, V_{GD}, V_{GS}	Drain–source, gate–drain, and gate–source voltages
V_{DS0}, V_{GS0}	Quiescent drain–source/gate–source voltage
$V_{\mathrm{D,max,RF}}$, $V_{\mathrm{D,min,RF}}$	Maximum/minimum RF-V_{DS}-voltage
$V_{\mathrm{GS},X}$	Dispersion corrected V_{GS}-voltages
$V_{\mathrm{GS,3}}^{psat}$, $V_{\mathrm{GS,3}}^{plin}$	Linearity parameters
V_{bgate}	Breakdown parameter in the LS-model
V_{dgt}	Gate–drain voltage function
V_{kl}	Voltage at device port k,l
V_{knee}	Knee voltage
V_{p}	Pinch-off voltage
V_{p2}	Doping correction to the threshold voltage
V_{thr}	Threshold voltage
W	Wafer bow
$W_{\mathrm{e}}, W_{\mathrm{eb}}$	Emitter-(base) width
W_{g}	Gate width
X_{EB},X_{E}	Thickness of the emitter, base
Y_{ij}	Y-parameter for $i, j = 1, 2$
Z_{ds}	Complex output conductance
Z_{ij}	Z-parameter for $i, j = 1, 2$
Z_0	Characteristic impedance
a, b, c, d, n	General parameters
$a_{\mathrm{gate-lag}}, a_{\mathrm{drain-lag}}$	Dispersion parameters for gate and drain-lag
$a_{\mathrm{gate,cw}}$,$a_{\mathrm{drain,cw}}$	Dispersion parameters comparing pulsed and cw
a_0, c_0	Lattice parameters
c_{300}	Heat capacity at 300 K
$c_{\mathrm{L,AB}}$	Nonlinear coefficient of the thermal conductivity of the ternary semiconductor

d	Thickness, length
d_{AlGaN}	Thickness of AlGaN
d_{eff}	Effective gate-to-channel separation
d_{doping}	Channel layer thickness
d_{sub}	Substrate diameter
e_{ij}	Piezoelectric coefficient
f_{T}	Current gain cut-off frequency
$f_{\mathrm{T,ext}}$	Extrinsic current gain cut-off frequency
f	Frequency
f_{c}	Frequency for $k = 1$
f_{c}	Lattice mismatch
f_{max}	Maximum frequency of oscillation
$f_{10\,dB}$	Maximum frequency which leaves 10 dB of power gain
$f(t, \mu, \sigma)_{\mathrm{lognorm}}$	Log-normal distribution function
$f(t, \mu, \sigma)_{\mathrm{norm}}$	Normal distribution function
f_1,f_2	Distribution function
g_{ds}	Output conductance
g'_{ds}m g''_{ds}	Derivatives of output conductance
$g_{\mathrm{ds,ext}}$	Extrinsic output conductance
$g_{\mathrm{ds,ext}}$(CW(RF or Pulsed))	Extrinsic output conductance for CW, RF, or pulsed operation
g_{m}	(Complex) transconductance
g'_{m}, g''_{m}	Derivatives of transconductance
g_{mi}	Intrinsic transconductance
$g_{\mathrm{m,max}}$	Maximum transconductance
h, $\hbar$	(Reduced) Planck constant
h_{21}	Current–gain
$h(t)$	Thermal response function in the time domain
i_{ds}	Intrinsic drain source current
i_{II}	Impact ionization current in the LS-model
$i_{\mathrm{d}}, i_{\mathrm{g}}$	Noise current at drain and gate
k_{B}	Boltzmann constant
k_{f}	Fukui factor
k_n, $k_{rel,n}$	Drain-lag dispersion model parameters
k	Stability factor
l_{fps}, l_{fpd}	Field-plate extension to the source and drain side
l_{gd}, l_{gs}	Gate-to-drain/-to-source separation
l_{gg}	Gate-to-gate pitch
l_{g}	Gate length
mb	Doping coefficient
m_e	Free electron mass

m_n	Effective electron mass
$m_n(\Gamma\text{-K})$, $m_n(\Gamma\text{-A})$, $m_n(\Gamma\text{-M})$	Effective electron mass at the Γ-K/A/M transition
$m_n(\text{X})$	Effective electron mass in X-valley
$m_{\nu,\text{AB}}$	Effective carrier mass of the semi-conductor $\text{A}_x\text{B}_{1-x}\text{N}$
$m_{n,\text{l}}$	Longitudinal electron mass
$m_{n,\text{t}}$	Transversal electron mass
m_p	Effective hole mass
$m_{p,\text{h}}$	Effective heavy hole mass
$m_{p,\text{l}}$	Light hole mass
$m_{p,\text{so}}$	Spin–orbit hole mass
m^*	Tunneling mass
$\boldsymbol{n}$	A normal vector
n	Electron concentration
n	Ideality factor
n	Refractive index
n_{channel}	Channel charge density
n_{i}	Intrinsic carrier concentration
n_{sheet}	Sheet carrier concentration
p	Hole concentration
q	Elementary charge
$q_{\text{bulk,traps}}$	Charge of bulk traps
q_{channel}	Channel charge
$q_{\text{diel,interface}}$	Interface charge
q_{doping}	Doping charge
q_{initial}	Dynamic charge
$q_{\text{semi,interfaces}}$	Charge at the semiconductor interfaces
t	Time
t	Thickness of the current-supporting layer
t_{ad}	Thickness of the adhesive
t_{sem}	Semiconductor thickness
t_{sub}	Substrate thickness
t_{subm}	Submount thickness
$\bar{v}_{\text{ds}}$,$\bar{v}_{\text{gs}}$	Static voltage components in dispersion model
v_{ds}, v_{d}	Intrinsic drain (source) voltage
v_{eff}	Effective carrier velocity
v_{gs}, v_{g}	Intrinsic gate (source) voltage
v_{peak}	Peak carrier velocity
v_{sat}	Saturated carrier velocity
x, y	Material composition parameter
y	Distance

List of Acronyms

2DEG	Two-Dimensional Electron Gas
3G	3rd generation (of mobile communication)
4G	4th generation (of mobile communication)
4H, 6H	Polytypes of SiC
AC	Alternating Current
ACLR	Adjacent Channel Leakage Ratio
ACPR	Adjacent Channel Power Ratio
ADS	Advanced Design System
AFM	Atomic Force Microscopy
AlN	Aluminum nitride
AESA	Active Electronically Scanned Array
ASIC	Application Specific Integrated Circuit
BCB	Bencocyclobutene
BEEM	Ballistic Electron Emission Spectroscopy
BGA	Ball-Grid-Array
BJT	Bipolar Junction Transistor
BN	Boron Nitride
BS	Backside Cooling
BV	Breakdown Voltage
CAD	Computer Aided Design
CAFM	Conductive Atomic Force Microscopy
CAIBE	Chemically-Assisted Ion Beam Etching
CAT-CVD	Catalytic Chemical Vapor Deposition
CAVET	Current Aperture Vertical Electron Transistor
CDMA	Code Division Multiple Access
CMOS	Complementary Metal Oxide Semiconductor
CMP	Chemical Mechanical Polishing
CTE	Coefficient of Thermal Expansion
CVD	Chemical Vapor Deposition
CW	Continuous Wave

c	cubic
DBF	Digital Beam-Forming
DC	Direct Current
DD	Drift-Diffusion
DLT(F)S	Deep Level Transient (Fourier) Spectroscopy
DHBT	Double Heterojunction Bipolar Transistor
DHFET	Double Heterojunction Field Effect Transistor
DHHEMT	Double Heterojunction High Electron Mobility Transistor
DOD	U.S. Department of Defense
DPD	Digital Predistortion
DRA	Driver Amplifier
EBIC	Electron-Beam Induced Current
ECR	Electron Cyclotron Resonance
ECMP	Electrochemical-Mechanical Polishing
EDGE	Enhanced Data Rates for GSM Evolution
EDX	Electron Diffraction
EER	Envelope Elimination and Restoration
ELO, ELOG, LEO	Epitaxial Lateral Overgrowth
ESD	Electrostatic Discharge
ET	Envelope-Tracking
EUV	Extreme Ultraviolet
EVM	Error Vector Magnitude
FC	Flip-Chip
FET	Field Effect Transistor
FIB	Focussed Ion Beam
FIT	Failures in Time
FOM	Figure-Of-Merit
GaAs	Gallium Arsenide
GaN	Gallium Nitride
GCPW	Grounded Coplanar-Waveguide
GSM	Global System for Mobile Communications
HBT	Heterojunction Bipolar Transistor
HCI	Hot Carrier Injection
HEMT	High Electron Mobility Transistor
HFET	Heterostructure Field Effect Transistor
HPA	High-Power Amplifier
HPSI	High-Purity Semi-Insulating (substrates)
HR	High-Resistivity
HTCC	High-Temperature Cofired Ceramics
HTCVD	High-Temperature Chemical Vapor Deposition
HVPE	Hydride Vapor Phase Epitaxy
IC	Integrated Circuit
ICP	Inductively Coupled Plasma
IDLDMOS	Interdigitated-Drain LDMOS

IF	Intermediate Frequency
II	Impact Ionization
IMPATT	IMPact Avalanche Transit Time
InAlN	Indium Aluminum Nitride
InAs	Indium Arsenide
InGaN	Indium Gallium Nitride
InN	Indium Nitride
JFET	Junction Field-Effect Transistor
LDMOS	Laterally diffused MOS
LED	Light-emitting Diode
LEEN	Low-Energy Electron-Excited Nanoscale Luminescence Spectroscopy
LNA	Low-Noise Amplifier
LO	Local Oscillator
LPCVD	Low-Pressure Chemical Vapor Deposition
LT	Low-Temperature
LTCC	Low-Temperature Cofired Ceramics
MAG	Maximum Available Gain
MBE	Molecular Beam Epitaxy
MC	Monte Carlo
MCM	Multi-Chip Module
MEMS	Micro-Electro-Mechanical Systems
MERFS	Micro Electromagnetic Radio Frequency System
MESFET	MEtal Semiconductor Field Effect Transistor
MHEMT	Metamorphic HEMT
MIC	Microwave Integrated Circuit
MIM	Metal–Insulator–Metal
MISFET	Metal Insulator Field Effect Transistor
MISHEMT	Metal Insulator Semiconductor HEMT
MMIC	Monolithic Microwave Integrated Circuit
MOCVD	Metal Organic Chemical Vapor Deposition
MOD	Ministry of Defense
MODFET	Modulation-Doped FET
MOMBE	Metal Organic Molecular Beam Epitaxy
MOS	Metal–Oxide–Semiconductor
MOSFET	Metal–Oxide–Semiconductor FET
MOSDHFET	Metal–Oxide Double Heterostructure FET
MOVPE	Metal Organic Vapor Phase Epitaxy
MSG	Maximum Stable Gain
MSL	Microstrip Line
MTBF	Mean Time Before Failure
MTTF	Mean Time to Failure
NBTI	Negative Bias Temperature Instability
NID	Non-Intentionally Doped
NiCr	Nickel Chromium

OFDM	Orthogonal Frequency-Division Multiplexing
ONO	Oxide–Nitride–Oxide
PA	Power Amplifier
PAE	Power-Added Efficiency
PAMBE	Plasma-Assisted Molecular Beam Epitaxy
PAR	Peak-to-Average Ratio
PAS	Positron Annihilation Spectroscopy
PCB	Printed Circuit Board
PCDE	Peak Code Domain Error
PEC	Photo-enhanced Electrochemical Etching
PECVD	Plasma-enhanced Chemical Vapor Deposition
PHEMT	Pseudomorphic HEMT
PIC	Polarization-Induced Charge
PL	Photoluminesce
PLM	Polarized Light Microscopy
PVT	Physical Vapor Deposition
RF	Radio Frequency
RIE	Reactive Ion Etching
RMS	Root-Mean Square
RTA	Rapid Thermal Annealing
Rx	Receiver
SAR	Synthetic Aperture Radar
SAW	Surface Acoustic Wave
SEM	Scanning Electron Microscopy
SH	Self-Heating
SHBT	Single Heterojunction Bipolar Transistor
SHFET	Single Heterojunction Field Effect Transistor
SHHEMT	Single Heterojunction High Electron Mobility Transistor
s.i., SI	Semi-Insulating
SiC	Silicon Carbide
SiCOI	Silicon Carbide on Insulator
SiCoSiC	Silicon Carbide on polySiC
SIMS	Secondary Ion Mass Spectroscopy
SiN	Silicon Nitride
SIP	System-In-Package
SIT	Static Induction Transistor
SKPM	Scanning Kelvin Probe Microscopy
SMD	Surface Mount Device
SoC	System on a Chip
SOI	Silicon On Insulator
SopSiC	Silicon on poly-crystalline SiC
SPDT	Single Pole Double Throw
SRPES	Synchrotron Radiation Photoemission Spectroscopy

SRH	Shockley–Read–Hall
SSPA	Solid-State Power Amplifier
STEM	Scanning Tunneling Electron Microscopy
TaN	Tantalum Nitride
TDD	Threading-Dislocation Density
TE	Thermionic Emission
TEM	Transmission Electron Microscopy
TLM	Transmission-Line Model
TMGa, TMAl, TMIn	TrimethylGallium, TriMethylAluminum, TriMethylIndium
T/R,TRX	Transmit/Receive
TWA	Traveling Wave Amplifier
TWTA	Traveling Wave Tube Amplifier
UWB	Ultra-Wide Band
VCO	Voltage-Controlled Oscillator
WBG	Wide BandGap
WBS	Wide Bandgap Semiconductor
WCDMA	Wideband Code Division Multiple Access
WiMAX	Worldwide interoperability For Microwave Access
Wz	Wurtzite
XRD	X-Ray Diffraction
Zb	Zincblende

1

Introduction

This monograph is devoted to the development of III-N semiconductor-based electronics for high-power and high-speed RF-applications. Material properties of these polar materials, the state-of-the-art of substrates, epitaxial growth, device and processing technology, modeling, and circuit integration, and examples are discussed. A full chapter is devoted to the critical aspect of device reliability. The work concludes with integration and packaging aspects specific to the new properties of III-N-based-circuits and subsystems.

In the second chapter, general material and transport properties, advantages, and theoretical electrical and thermal limits are presented. Further, the state-of-the-art for nitride-based substrates, materials, electronic devices, and circuits are reviewed systematically.

For epitaxial growth, both the aluminum and indium-based binary and ternary compounds are described with emphasis on AlGaN/GaN and In–Ga–N-based heterostructure systems in Chapter 3. Epitaxial growth techniques such as molecular beam epitaxy (MBE) and metal organic chemical vapor deposition (MOCVD) are analyzed systematically. Nitride-specific material characterization, doping, and material quality issues are analyzed. Substrate properties are reviewed systematically with respect to electronic requirements.

Currently a major focus of development is devoted to high electron mobility transistors (HEMTs) with gate lengths down to 30 nm and cut-off frequencies up to 190 GHz. Thus, for this class of devices, specific field-effect transistor problems such as Schottky and ohmic contacts, and lithography of optically transparent materials are discussed. State-of-the art recess processes and passivation technologies are analyzed. Bipolar device technology issues are reviewed.

In the device modeling and characterization Chapter 5, DC, small-signal, and noise characterization and modeling are presented with respect to nitride-specific questions. As frequency dispersion is a major source of performance and device degradation, the characterization and reduction of dispersion involving pulsed-characterization and other advanced techniques are dis-

cussed. Large-signal characterization and modeling are discussed for nitride devices, including the modeling of contacts, diodes, dispersion, and thermal aspects.

Chapter 6 discusses circuit examples for high-power RF amplifiers with a focus on increased impedance, thermal management, and high RF-power management between 0.5 and 100 GHz. Low-noise amplifiers are presented and analyzed for high-dynamic range, robustness, and high linearity. The last section of the chapter treats other circuits functions such as mixers and oscillators. Again, nitride-specific advantages and challenges are investigated.

In Chapter 7, nitride-specific device and circuit reliability issues and device failure mechanisms are analyzed and described systematically. The last chapter describes integration and packaging considerations, thermal-mounting and thermal-packaging considerations, for state-of-the-art amplifiers, and subsystems.

2

III-N Materials, and the State-of-the-Art of Devices and Circuits

In this chapter, general material and transport properties, advantages, and theoretical electrical and thermal limits of nitride semiconductors are presented with respect to electronic applications. This chapter further provides an overview of substrate materials. The state-of-the-art for nitride-based materials, electronic devices, and circuits are reviewed systematically. The last section defines application-specific requirements on nitride semiconductor devices from a more system oriented point of view. The chapter concludes with a number of problems.

2.1 State-of-the-Art of Materials Research

A systematic overview of the material properties is given in the following. For a systematic introduction, Fig. 2.1 depicts the bandgap at a lattice temperature of 300 K for various semiconductor materials as a function of lattice constant. The selection of the specific material constant as lattice constant in noncentrosymmetric materials may be arbitrary, however, is useful for a systematic introduction. With the bandgap of InN recently suggested to be about 0.8 eV and the bandgap of AlN to be 6.2 eV at room temperature, the III-N material system covers a very broad range of energies and thus emission wave lengths from the infrared to the deep ultraviolet unchallenged by any other available material. Electronically, a very broad range of bandgap energies is found resulting in extremely high bulk material breakdown voltages, which can be traded in for low-effective mass and high mobility of GaN with $m_n = 0.2\,m_e$, or even of InN with $m_n = 0.11\,m_e$ (potentially even $m_n = 0.04\,m_e$ [2.122]) by changing the material compositions in the heterostructures. At the same time, a second trade-off is imminent and different from any other semiconductor material system. Due to the strong polar material properties, the modification of the material composition results in dramatic modifications of the polar crystal properties, and thus of available

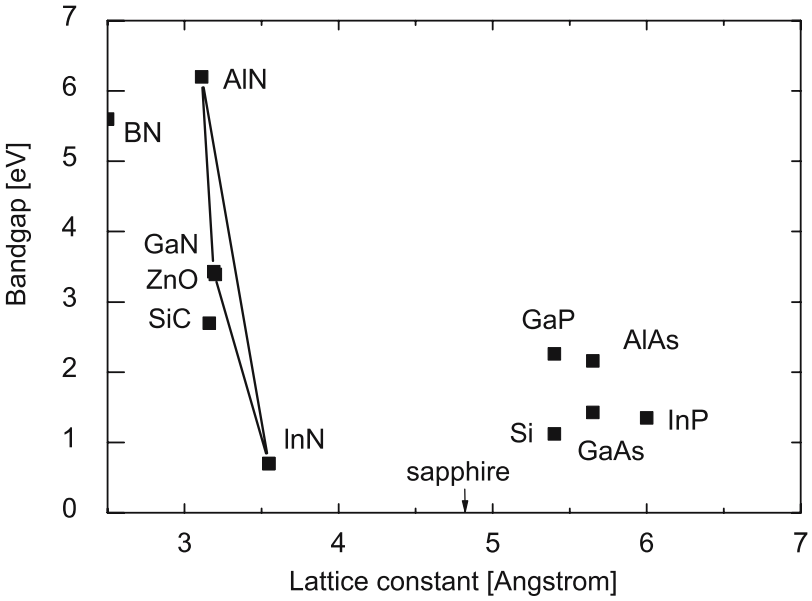

Fig. 2.1. Bandgap energy at $T_L = 300\,K$ as a function of lattice constant of III-N semiconductors: Other III-V semiconductors are given for comparison

carrier concentrations obtained at the interfaces and thus available in the devices. Thus, and in some respect very similar to silicon, the huge success of III-N material is not mainly due to the intrinsic bulk material transport properties (especially the p-material properties do not compare well with n-properties in III-N materials), but due to the interface properties. In the case of silicon, the success is based on the formation of a native oxide which can be optimized and used tremendously, e.g., [2.411], and is recently replaced by other dielectrics, which also are well behaved on silicon, e.g., [2.136, 2.145].

In the case of III-N heterostructures, the interfaces allow for the formation of n-channels and intrinsically provide extremely high carrier concentrations $\geq 10^{13}\,cm^{-2}$ through polarization engineering without further impurity doping. On the contrary, and unlike silicon, the semiconductor–dielectric interfaces remain a challenge in the III-N world, as suitable interfaces can be formed from a practical point of view, however, these interfaces and their long term behavior are not well understood mainly due to the high-sheet charge concentrations.

2.1.1 Binary Materials

The binaries of the elements Al–In–Ga–B–N are the basic materials for the semiconductor material class named Nitrides: gallium nitride (GaN), aluminum nitride (AlN), indium nitride (InN), and boron nitride (BN). Epi-

taxially grown silicon nitride (SiN), although not of crystalline quality, may be added from time to time. Boron nitride (BN) is still relatively immature as a semiconductor material [2.99]. Initial results on the material and device level are available [2.99], featuring the especially good thermal conductivity of BN, second only to diamond when semiconductor materials are compared. Good overview papers and collections are available, with a focus also on optoelectronic and general material properties, and, e.g., in [2.100, 2.101, 2.244, 2.315, 2.324, 2.369, 2.389]. Laser diodes are particularly addressed in [2.323]. The properties of SiN and SiO_2 are reviewed, e.g., in [2.440].

Crystal Structures for Electronic Applications

The III-N semiconductors can be found in three common crystal structures:

- Wurtzite
- Zincblende
- Rock salt

At room temperature GaN, AlN, and InN are found in the wurtzite structure, while BN prevails mostly in the cubic structure. The zincblende structure can also be found for GaN and InN for thin films, while for AlN no stable zincblende phase has yet been detected [2.99]. However, this work addresses also some mostly theoretical work on Zb–AlN. The rock salt phase is of no importance to electronic devices so far. In the wurtzite structure the growth is typically performed along the *c*-axis. Recently, growth along the m-plane has been reported [2.61, 2.342], as the resulting nonpolar material has a positive influence on diodes efficiency in optoelectronics.

Gallium Nitride (GaN)

Gallium Nitride (GaN) is the basic material of this material class which is typically used for all device layers requiring fast carrier transport with a high breakdown voltage. GaN is used as the channel material in various FETs and also as the base material in AlGaN/GaN HBTs, e.g., [2.311]. Most of the ohmic contact layers in any device incorporate binary n-doped and p-doped GaN. GaN can further be grown as a semi-insulating material with growth parameters close to those of the semiconducting layers.

Mechanical and Optical Properties

The crystal structure and the mechanical and thermal properties of GaN are discussed in a number of publications, e.g., in [2.4, 2.244, 2.315, 2.389]. The data of all III-N binaries are also compiled in table form in the Appendix. As an initial quantity, Table 2.1 compiles the data on the mass density. The Vickers hardness and fracture toughness of bulk GaN in comparison to other semiconductors are given in [2.92]. More recent results are presented in [2.524]. Table 2.2 compares the values of the hardness H and fracture toughness K_C.

Table 2.1. Mass density of III-N and other semiconductor materials

Material	GaN	AlN	InN	BN	Si	Ref.
Mass density ($\mathrm{g\,cm^{-3}}$)	6.1	3.23	6.81	3.48	2.33	[2.17, 2.99, 2.443]

Wz wurtzite, *Zb* zincblende, *c* cubic, *d* diamond

Table 2.2. Vickers hardness H and fracture toughness K_C of III-N and other semiconductor materials

Material	GaN	AlN	InN	BN	SiC	Si	Ref.
H (GPa)	12	14	11.2	55–65	33	9	[2.92, 2.451]
K_C ($\mathrm{MPa\,m^{1/2}}$)	0.8	2.6	–	–	3.3	0.7	[2.92, 2.244]

Table 2.3. Elastic constants of wurtzite III-N semiconductors and other materials

	GaN (Wz)	AlN (Wz)	InN (Wz)	BN (c)	Ref.
C_{11} (GPa)	390	396	223	831	[2.99, 2.275, 2.372, 2.449, 2.485]
C_{33} (GPa)	398	373	200	–	[2.99, 2.275, 2.372, 2.449, 2.485]
C_{44} (GPa)	105	116	48	450	[2.372, 2.451, 2.485]
C_{12} (GPa)	145	137	115	190	[2.99, 2.275, 2.372, 2.449, 2.485]
C_{13} (GPa)	106	108	92	–	[2.275, 2.372, 2.449, 2.485]

Wz wurtzite, *c* cubic

Table 2.4. Elastic constants of zincblende III-N semiconductors

		GaN (Zb)	AlN (Zb)	InN (Zb)	BN (c)	Si	Ref.
C_{11}	(GPa)	293	304	187	820	165.8	[2.244, 2.371, 2.485]
C_{44}	(GPa)	155	193	86	480	79.6	[2.244, 2.371, 2.485]
C_{12}	(GPa)	159	160	125	190	63.9	[2.244, 2.371, 2.485]

Wz wurtzite, *Zb* zincblende, *c* cubic

Table 2.5. Coefficients of thermal expansion (CTE) of III-N semiconductors and other materials at room temperature

	GaN (Wz)	GaN (Sa)	AlN (p)	InN (p)	BN (c)	SiC	Sap.	Si	Ref.
α_a ($10^{-6}K^{-1}$)	3.1	3.8	2.9	3.6	1.15	3.2	4.3	2.6	[2.99, 2.222, 2.243]
α_c ($10^{-6}K^{-1}$)	2.8	2.9	3.4	2.6	–	3.2	3.2	2.6	[2.222, 2.243]

Wz wurtzite, *Sa* epitaxially on sapphire substrate, *c* cubic, *p* powder

c-BN is a particularly hard material, while GaN, AlN, and InN have nearly the same hardness. This hardness makes c-BN attractive in various ceramic materials. The elastic constants of wurtzite gallium nitride determined by Brillouin scattering are reported, for example, in [2.372] and are compiled in Table 2.3. A prediction of the high-temperature elastic constants of GaN, AlN, and InN is given in [2.381]. Deduced from this, a bulk modulus B_0 of GaN is found to be 210 GPa. For BN, a comparison of the different calculated and measured values is given in [2.99]. First principle calculations of the properties of zincblende AlN and GaN are given in [2.177]. The elastic constants of the zincblende phase are compiled in Table 2.4. The pressure dependence of the elastic constants of zincblende BN, AlN, GaN, and InN is analyzed in [2.178].

The linear coefficients of thermal expansion (CTE) at room temperature and at elevated temperatures are important for the growth. Those of wurtzite GaN have been measured between room temperature and $\geq$750 K for both bulk GaN and epitaxial layers grown on sapphire, e.g., in [2.243]. The data are compiled in Table 2.5. Table 2.5 further compares the CTE of III-N semiconductors to silicon carbide and other typical substrates materials. The differences in CTE and its temperature dependence have a similar impact to layer growth of heterostructures as the lattice constants, as discussed in Chapter 3. The thermal conductivity of GaN was initially reported in [2.423] and many of the references date back to this publication. More recent measurements, especially as function of dislocation density in thin layers, can be found in [2.120,2.216,2.264] and are discussed later with respect to the modeling and the importance of the crystalline quality. The data are compiled in Table 2.16.

Dielectric Constants

Compiling the basic dielectric properties, Table 2.6 gives both the static and the high-frequency dielectric constants. The dielectric constant of GaN is slightly lower than in silicon and GaAs (not shown). InN has the highest values of the three binary materials.

Overviews of further optical functions of GaN such as the refractive index are given in [2.3,2.298]. The absorption spectrum of GaN at room temperature and the absorption coefficient are presented in [2.64].

Table 2.6. Dielectric constants of III-N and other semiconductor materials

Material	GaN (Wz)	AlN (Wz)	InN (Wz)	GaN (Zb)	BN (c)	Si	Ref.
ε_r	9.5 $\perp$, 10.4 $\parallel$	8.5	15.3	9.5	7.1	11.9	[2.3, 2.64, 2.492]
ε_r^{inf}	5.5	4.77	8.4	5.35	4.5	–	[2.3, 2.64, 2.492]

Wz wurtzite, *Zb* zincblende, and *c* cubic

Basic Transport Properties

Electronic transport in GaN is mostly understood, but a number of issues remain for further research. These include, e.g., the maximum carrier velocity v_{peak} in bulk material and at heterointerfaces, which are discussed later. General electrical properties of GaN, as well as AlN and $\mathrm{Al}_x\mathrm{Ga}_{1-x}\mathrm{N}$, are compiled in [2.123]. An early, but accurate estimate of the carrier concentration dependence of the bulk mobility in GaN, InN, and AlN using the variational method is given in [2.64]. Based on more recent data, a mobility and carrier vs. doping concentration analysis for wurtzite MOCVD-grown bulk GaN is provided in [2.259]. Both donor and acceptor concentrations in the order of $10^{17}\,\mathrm{cm}^{-3}$ are extracted. A specific mobility model for bulk GaN including the dependence on the free electron concentration is given in [2.308]; however, newer experimental results require an update of the actual parameters.

Table 2.7. Comparison of the low-field mobility values in various III-N bulk and 2DEG materials

Material	n/p	T_{L} (K)	$N_{\mathrm{D}}/N_{\mathrm{A}}$ (cm^{-3})	μ ($\mathrm{cm}^2\,\mathrm{V}^{-1}\,\mathrm{s}^{-1}$)	Method	Ref.
GaN (Wz)	n	300	$N_{\mathrm{D}} = 1 \times 10^{17}$	990	MC	[2.113]
GaN (Wz)	n	450	$N_{\mathrm{D}} = 1 \times 10^{17}$	391	MC	[2.113]
GaN (Wz)	n	600	$N_{\mathrm{D}} = 1 \times 10^{17}$	215	MC	[2.113]
GaN (Wz)	p	300	$N_{\mathrm{A}} = 3.6 \times 10^{16}$	150	meas.	[2.123]
GaN (Wz)	n 2DEG	300	0	2,000	MC	[2.337]
GaN (Wz)	n	77	$N_{\mathrm{D}} = 1 \times 10^{16}$	6,000	VP	[2.64]
GaN (Zb)	n	300	$N_{\mathrm{D}} = 1 \times 10^{17}$	1,100	MC	[2.17]
GaN (Zb)	n 2DEG	300	0	2,100	MC	[2.337]
GaN (Zb)	p	300	$N_{\mathrm{A}} = 1 \times 10^{13}$	350	meas.	[2.21]
AlN (Wz)	n	300	$N_{\mathrm{D}} = 1 \times 10^{17}$	135	MC	[2.349]
AlN (Wz)	n	77	$N_{\mathrm{D}} = 1 \times 10^{16}$	2,000	VP	[2.64]
AlN (Zb)	n	300	0	200	MC	[2.17]
AlN (Zb)	n	100	0	400	MC	[2.17]
InN (Wz)	n	300	$N_{\mathrm{D}} = 1 \times 10^{17}$	3,000	MC	[2.35]
InN (Wz)	n	300	$N_{\mathrm{D}} = 1.5 \times 10^{17}$	3,570	meas.	[2.114]
InN (Wz)	n	77	$N_{\mathrm{D}} = 1 \times 10^{16}$	30,000	VP	[2.64]
InN (Zb)	n	100	$N_{\mathrm{D}} = 1 \times 10^{17}$	9,000	MC	[2.17]
BN (c)	p	300	$N_{\mathrm{A}} = 5 \times 10^{18}$	500	meas.	[2.253]

Wz wurtzite, *Zb* zincblende, *c* cubic, *VP* variational principle, *MC* Monte Carlo, *meas.* measured

Low-Field Mobility

Several predictions and measurements are available for obtaining estimates for the maximum low-field mobility in both bulk and 2DEG electron gas. Table 2.7 compiles the data of the low-field mobility with respect to temperature and impurity dependence of the mobility in III-N bulk materials. The maximum values from [2.64] are given for completely uncompensated material.

Recent advances in material growth show great improvements in channel mobility of optimized AlGaN/GaN 2DEG channel-layer material with Hall mobility values of up to $2{,}000\,\mathrm{cm^2\,V^{-1}\,s^{-1}}$ [2.435] at room temperature in agreement with theoretical predictions [2.337]. For the analysis of the mobility in bulk and 2DEG-GaN, the temperature dependence is plotted in Fig. 2.2 taken from [2.37] and data therein. The effects to influence mobility include:

- Phonon scattering by acoustic and optical phonons
- Ionized impurity scattering [2.37] at both background impurities and surface donors
- Threading dislocations [2.258, 2.329, 2.435]
- Alloy scattering [2.34, 2.414]

The maximum drift mobility of wurtzite bulk GaN is about $1{,}100\,\mathrm{cm^2\,V^{-1}\,s^{-1}}$. The hole mobility in bulk GaN is much lower with maximum values of $175\,\mathrm{cm^2\,V^{-1}\,s^{-1}}$. The reduced impurity scattering in 2DEG channels at

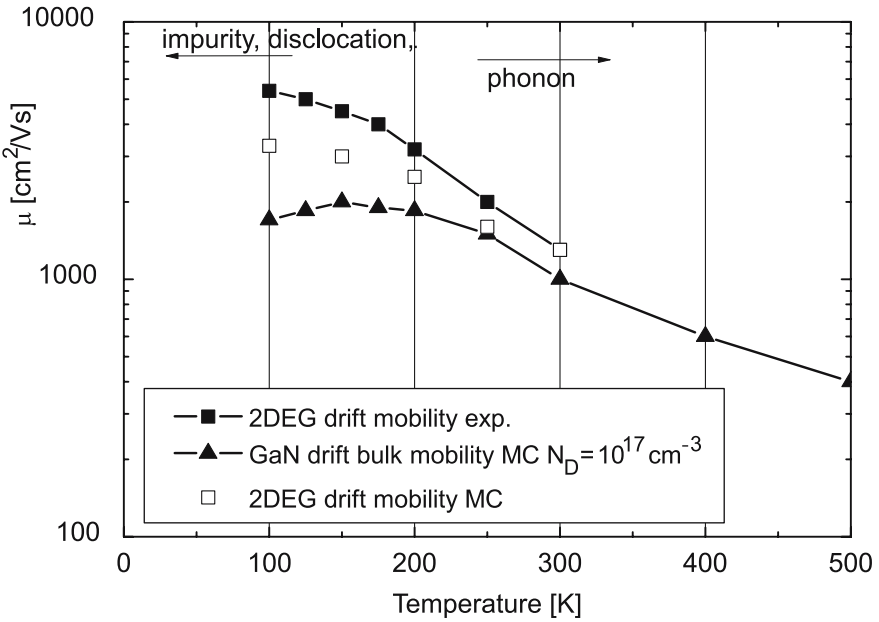

Fig. 2.2. Drift mobility as a function of lattice-temperature T_L for bulk GaN and 2DEG-GaN depicting the different limiting effects from [2.37, 2.329]

very low surface scattering levels yield 2DEG-mobility values of up to $2{,}000\,\mathrm{cm^2\,V^{-1}\,s^{-1}}$ for both wurtzite and zincblende material. A theory of charged dislocation scattering in GaN is given [2.258]. The fit of the temperature-dependent Hall data can be correlated with the dislocations observed by TEM. The impact of threading dislocations on the transverse mobility in GaN is further discussed in [2.493]. The model explains the impact of trap occupancy and related scattering on the mobility at different doping levels. Alloy disorder is a limiting factor to transport at GaN heterointerfaces, as discussed in [2.414]. Further analysis is provided in Chapter 3. AlN is an insulator due to the high activation energy of the donors and the large bandgap. The theoretical low-field mobility of AlN is discussed in [2.17]. It is found to be phonon-limited with the electron mobility values given in Table 2.7. Theoretical values for the drift mobility of $135\,\mathrm{cm^2\,V^{-1}\,s^{-1}}$ and $200\,\mathrm{cm^2\,V^{-1}\,s^{-1}}$ for fully uncompensated material have been found. Similar to InN, the hole transport properties of AlN are not understood very well. The predicted low-field drift mobility of InN at room temperature is found to be as high as $3{,}000\,\mathrm{cm^2\,V^{-1}\,s^{-1}}$ in [2.35] and $3{,}700\,\mathrm{cm^2\,V^{-1}\,s^{-1}}$ in [2.17]. At 100 K, a maximum low-field mobility as high as $9{,}000\,\mathrm{cm^2\,V^{-1}\,s^{-1}}$ is predicted for zincblende InN material [2.17]. Variational principle calculations leads to predictions of $30{,}000\,\mathrm{cm^2\,V^{-1}\,s^{-1}}$ at 77 K for completely uncompensated material at low impurity concentrations of $10^{16}\,\mathrm{cm^{-3}}$. Again, hole transport in InN is not well understood due to the lack of proper p-doping [2.170].

High-Field Transport

Several MC calculations of the velocity-field characteristics of wurtzite GaN considering the high-field transport are available and given, e.g., in [2.37, 2.121]. There is a significant discussion on the extraction of delay times in HFETs and resulting carrier velocities, which disagree with the MC calculations, see also Sect. 2.2.7. Table 2.8 compiles the bulk saturation velocity and critical field parameters from various sources. The comparison reveals the increase of both the saturation velocity v_{sat} and the critical field E_{crit} compared to other high-speed materials such as silicon, GaAs, and SiC. Peak velocity values as high as $3 \times 10^7\,\mathrm{cm\,s^{-1}}$ are found for electrons in GaN. The differences between wurtzite and zincblende semiconductors are found to be insignificant. AlN has a very high critical field in agreement with the high bandgap energy, whereas the critical field of InN is lower than in GaN. The predicted electron peak velocity in InN can be as high as $4 \times 10^7\,\mathrm{cm\,s^{-1}}$.

Apart from bulk material, MC simulations in 2DEG AlGaN/GaN channels including hot-phonon and degeneracy effects are provided in [2.380] by a combined MC and Schrödinger–Poisson analysis. The wavefunctions for the confined electrons are calculated. The simulation suggests that the degeneracy in the 2DEG reduces the electron drift velocity, while hot phonons reduce the drift velocity and increase the electron energy relaxation time. The energy relaxation time at RT extract by MC simulation amounts to

Table 2.8. Comparison of the velocity-field characteristics in various bulk materials

Material	n/p	T_L (K)	E_{crit} (kV cm^{-1})	v_{peak} (10^7 cm s^{-1})	v_{sat} (10^7 cm s^{-1})	N_D/N_A (cm^{-3})	Ref.
GaN (Wz)	n	300	175	2.5	–	2×10^{16}	[2.500]
GaN (Wz)	n	300	150	2.7	2.5	1×10^{16}	[2.37]
GaN (Wz)	n	300	140	2.9	1.8	1×10^{17}	[2.121]
GaN (Wz)	n	77	150	3.2	2.7	1×10^{16}	[2.37]
GaN (Wz)	p	300	–	–	0.48	–	[2.286]
GaN (Zb)	n	300	145	2.6	1.34	1×10^{17}	[2.17]
GaN (Zb)	p	300	–	–	0.92	–	[2.286]
AlN (Wz)	n	300	450	1.7	1.4	1×10^{17}	[2.121, 2.349]
AlN (Wz)	n	300	447	2.3	2.16	1×10^{17}	[2.113]
AlN (Wz)	p	300	–	–	–	–	–
AlN (Zb)	n	300	550	1.8	1.59	1×10^{17}	[2.17]
AlN (Zb)	p	300	–	–	–	–	–
InN (Wz)	n	300	65	4.2	1.8	1×10^{17}	[2.121]
InN (Wz)	n	300	52	3.4	–	1×10^{17}	[2.113]
InN (Zb)	n	300	45	2.9	1.4	1×10^{17}	[2.17]
InN (Zb)	p	300	–	–	–	–	–

Wz wurtzite, *Zb* zincblende, *c* cubic

0.3 ps at 10 kV cm^{-1} [2.380]. Experimental determination of the hot electron energy relaxation time in MBE-grown n-GaN is presented in [2.521]. The extracted value amounts to 0.2 ps at at a carrier concentration of 10^{18} cm^{-3}. Similar field-dependent investigations in AlGaN/GaN heterostructures based on microwave noise are given in [2.281]. RT data yields energy relaxation times of 0.3 ps at 10 kV cm^{-1} and 1 ps at 2 kV cm^{-1}. The transient electron transport based on MC simulations in wurtzite GaN, InN, and AlN is discussed in [2.121]. In the transient situation very high theoretical overshoot values are observed. However, the paper also depicts the trade-off between transient overshoot and saturated velocity in bulk FET-like transient transport.

Band Structure of GaN

The band structure of GaN has been analyzed in a number of publications, e.g., in [2.108,2.127,2.128,2.238,2.522]. However, it is not yet fully understood, especially with respect to the higher energy bands. A comprehensive overview of the band parameters of wurtzite and zincblende GaN, AlN, and InN is given in [2.485] in a continuation of the great III-V overview in [2.486]. A consistent set of parameters is presented for both the wurtzite and zincblende binary III-N materials. From an experimental point of view, absorption coefficient,

energy gap, exciton binding energy, and recombination lifetime of Wz–GaN are measured and reported in [2.317]. From these both bandgap, exciton energies, and radiative constants can be derived.

Table 2.9 compiles available mass parameters from band structure calculations and measurements. Various predictions exist for the effective electron mass in GaN, e.g., in [2.128]. The conduction band electron effective mass in wurtzite GaN is measured to be $0.2\,m_e$, as reported in [2.91]. The effective mass parameters are further collected from the band structure calculations in [2.127, 2.128, 2.238, 2.486]. The heavy hole masses $m_{p,\mathrm{h}}$ are further distinguished along the x- and z-direction. The hole effective mass in p-GaN and the influence of band splitting and band anisotropy on free hole statistics

Table 2.9. Comparison of the effective mass parameters in various III-N semiconductor materials

	m_n (m_e)	$m_n(\Gamma-K)$ (m_e)	$m_n(\Gamma-A)$ (m_e)	$m_n(\Gamma-M)$ (m_e)	Ref.
GaN (Wz)	0.2	0.36	0.27	0.33	[2.91]
AlN (Wz)	0.48	0.42	0.33	0.40	[2.349]
InN (Wz)	0.11 (0.05)	–	–	–	[2.122, 2.486]

	$m_n(\Gamma)$ (m_e)	$m_{n,\mathrm{l}}(X)$ (m_e)	$m_{n,\mathrm{t}}(X)$ (m_e)	Ref.
GaN (Zb)	0.15	0.5	0.30	[2.108, 2.485]
AlN (Zb)	0.25	0.53	0.31	[2.108, 2.485]
InN (Zb)	0.07–0.11	0.48	0.27	[2.485]

	$m_{p,\mathrm{h}}$ (m_e)	$m_{p,\mathrm{l}}$ (m_e)	$m_{p,\mathrm{so}}$ (m_e)	Ref.
GaN (Wz)	1.4	0.3	0.6	[2.108, 2.244]
AlN (Wz)	3.52 (z)	3.53 (z)	0.25 (z)	[2.108, 2.244]
AlN (Wz)	10.42 (x)	0.24 (x)	3.81 (x)	[2.108, 2.244]
InN (Wz)	1.63	0.27	0.65	[2.108, 2.244]

		$m_{p,\mathrm{h}}$ (m_e)	$m_{p,\mathrm{l}}$ (m_e)	$m_{p,\mathrm{so}}$ (m_e)	Ref.
GaN (Zb)	[100]	0.74	0.21	0.33	[2.108]
GaN (Zb)	[111]	1.82	0.18	0.33	[2.108]
GaN (Zb)	[110]	1.51	0.19	0.33	[2.108]
AlN (Zb)	[100]	1.02	0.35	0.51	[2.108]
AlN (Zb)	[111]	2.85	0.30	0.51	[2.108]
AlN (Zb)	[110]	2.16	0.31	0.51	[2.108]

Wz wurtzite, *Zb* zincblende

in wurtzite GaN are discussed in [2.400]. The degeneracy effects are strong and require detailed investigations to obtain the effective hole mass at the particular density-of-states.

Bandgap Energies

The bandgap energy parameters of different crystal structures in III-N materials are compared in Table 2.10. Further, the intervalley separation energies in k-space are of practical importance for the high-field transport of electrons and holes. They are compiled in Table 2.11 for both wurtzite and zincblende structures. The uncertainty of the band structure and energy gap prevails specifically for AlN and InN for the higher bands.

The data of wurtzite GaN and AlN are based on the first principle calculations in [2.441] and the erratum [2.442]. At heterointerfaces between two semiconductors, the energy band discontinuities and bandgap alignments are of high importance, as they determine the energy barriers which the carriers have to surmount. All III-N materials lead to so-called type-I transitions. However, in conventional heterostructures, the alignments are symmetrical with respect to the growth order starting from the substrate. In highly polar semiconductors, such as the III-N material system, this is not necessarily the case, due to the strain effects depending on the substrate (bottom), and the resulting strain and thus polarization charge in the thin top layer. The valence band discontinuities for GaN, AlN, and InN have been complied, e.g., in [2.275]. The valence band alignment energies are found for the three binary materials, as given in Table 2.12. The additional transitions toward ternary material are also discussed later. BN is not included in this comparison, as the cubic phase BN cannot be grown lattice-matched to the other materials.

Table 2.10. Comparison of the bandgap parameters in various bulk materials at 300 K

		(Wz)	Ref.			(Zb)	Ref.
GaN $E_{g,\Gamma 1}$	(eV)	3.43	[2.121]	$E_{g,\Gamma}$	(eV)	3.38, 3.1, 3.2	[2.108]
GaN $E_{g,\Gamma 3}$	(eV)	5.29	[2.121]	$E_{g,X}$	(eV)	4.57, 4.7	[2.108]
GaN $E_{g,L-M}$	(eV)	5.49	[2.121]	$E_{g,L}$	(eV)	5.64, 6.2	[2.108]
AlN $E_{g,\Gamma 1}$	(eV)	6.2, 6.12	[2.121, 2.245]	$E_{g,\Gamma}$	(eV)	5.94, 6.0	[2.108]
AlN $E_{g,L-M}$	(eV)	6.9	[2.121]	$E_{g,X}$	(eV)	5.1, 4.9	[2.108]
AlN $E_{g,G-A}$	(eV)	7.2	[2.121]	$E_{g,L}$	(eV)	9.42, 9.3	[2.108]
InN $E_{g,\Gamma 1}$	(eV)	0.77	[2.501]	$E_{g,\Gamma}$	(eV)	0.75	[2.486]
InN $E_{g,G-A}$	(eV)	4.09	[2.121]	$E_{g,X}$	(eV)	2.486	[2.486]
InN $E_{g,\Gamma 3}$	(eV)	4.49	[2.121]	$E_{g,L}$	(eV)	5.79	[2.486]

Wz wurtzite, *Zb* zincblende

Table 2.11. Comparison of the intervalley separation energies in various bulk materials at 300 K

		(Wz)	Ref.			(Zb)	Ref.
GaN –	(eV)	–	–	Γ	(eV)	–	–
GaN $\Gamma - 3$	(eV)	1.9	[2.121]	$\Gamma - X$	(eV)	1.4	[2.17, 2.244]
GaN $L - M$	(eV)	2.1	[2.121]	$\Gamma - L$	(eV)	1.6–1.9	[2.244]
AlN Γ	(eV)	–	–	–	(eV)	–	
AlN $\Gamma - (L - M)$	(eV)	0.7	[2.121, 2.441]	–	(eV)	–	
AlN $\Gamma - K$	(eV)	1.0	[2.121, 2.441]	–	(eV)	–	
InN –	(eV)	–	–		(eV)	–	
InN $\Gamma - (M - L)$	(eV)	2.9–3.9	[2.244]		(eV)	–	
InN $\Gamma - A$	(eV)	0.7–2.7	[2.244]		(eV)	–	

Wz wurtzite, *Zb* zincblende

Table 2.12. Comparison of the bandgap alignment parameters in various bulk materials at 300 K

Top	Bottom (eV)	GaN (Wz)	AlN (Wz)	InN (Wz)	Ref.
GaN	(Wz)	0	0.7	1.05	[2.275]
AlN	(Wz)	0.7	0	1.81	[2.275]
InN	(Wz)	1.05	1.81	0	[2.275]
Top	Bottom (eV)	GaN (Zb)	AlN (Zb)	InN (Zb)	Ref.
GaN	(Zb)	0	0.85	0.51	[2.324]
AlN	(Zb)	0.85	0	1.09	[2.324]
InN	(Zb)	0.51	1.09	0	[2.324]

Wz wurtzite, *Zb* zincblende

Further empirical pseudopotential calculations of wurtzite GaN and InN are given in [2.522]. For the complete band structure, a nonlocal pseudopotential calculation of the III-nitride wurtzite phase materials system is performed in [2.128] for binary compounds such as GaN, AlN, and InN. Band structure calculations of wurtzite-type GaN and AlN are given in [2.298, 2.441]. Particularly the complicated valence band structure and the effective mass parameters of the wurtzite nitrides are obtained. The cubic approximation is found to be fairly successful in the analysis for the valence-band structures of the wurtzite-type nitrides.

Table 2.13. Comparison of the direct recombination parameters in various bulk materials at 300 K

	GaN (Wz)		AlN (Wz)		InN (Wz)	
B ($\mathrm{cm^3\,s^{-1}}$)	1.1×10^{-8}	[2.317]	0.4×10^{-10}	[2.489]	2×10^{-10}	[2.533]

Wz wurtzite

The band structure in zincblende GaN, AlN, and AlGaN is described in [2.108]. Particularly, the energies of Γ, X, and L valley of $Al_xGa_{1-x}N$ as a function of mole fraction x of are calculated.

Table 2.13 gives the direct recombination parameters of the III-N semiconductors for the direct band structure. As can be derived, the direct recombination in GaN is very strong and about an order of magnitude higher than, e.g., in GaAs.

Aluminum Nitride (AlN)

Second to GaN, AlN is the most important binary material in the III-N material family for electronic applications and is mostly used as its ternary compound $Al_xGa_{1-x}N$, e.g., in barriers heterostructures. It is characterized to be an insulator due to the high-bandgap energy and the high-activation energy of donors. Binary AlN is usually grown nucleation layer to start the growth on s.i. SiC or sapphire substrates, e.g., [2.96] and as an interlayer at the channel/barrier interface, e.g., [2.66].

Mechanical and Optical Properties

Basic properties such as the crystal structure, mechanical properties, and thermal properties of AlN are compiled in [2.287]. The mass density of AlN is much smaller than in GaN or InN, as given in Table 2.1. As depicted in Tables 2.2 and 2.3, thermal expansion and Vickers hardness of AlN are relatively similar to those of GaN. Elastic constants of AlN are given for the wurtzite phase in Table 2.3 and for the zincblende phase in Table 2.4.

The intrinsic thermal conductivity of AlN is determined in [2.428]. Its high-thermal conductivity is better than that of any other semiconductor apart from BN, SiC, and diamond, as is compiled in Table 2.16. This makes AlN a potentially attractive substrate material. The optical functions, such as the refractive index n, of AlN are given in [2.287]. The optical functions are also compiled in [2.260], including the dielectric functions and the absorption functions.

Basic Carrier Transport Properties

Although not of primary importance to most devices except in very thin layers close to the channel, transport in AlN is relatively well investigated

by MC simulations, also with respect to the understanding of the transport in $Al_xGa_{1-x}N$ for various material compositions x. An early compilation of the transport data of $Al_xGa_{1-x}N$ and AlN is given in [2.123], yielding the low mobility of wurtzite AlN for both n- and p-type material, as given in Table 2.8. The low-field electron mobility of AlN is calculated to be $135\,cm^2\,V^{-1}\,s^{-1}$ at room temperature and at a doping concentration of $10^{17}cm^{-3}$.

High-Field Transport

The electron high-field transport in wurtzite AlN is investigated by MC simulations in [2.349]. Further MC simulations on the transient transport in AlN are given in [2.121]. The characteristics are determined by the relatively high-effective electron mass of $0.48\,m_e$, the large bandgap of $\approx$6.2 eV, and the very small intervalley separation. The resulting velocity-field characteristic yields a very high critical field of $450\,kV\,cm^{-1}$ [2.349], as shown in Table 2.7. The saturation velocity in AlN reaches $1.4\times10^7\,cm\,s^{-1}$ at room temperature, while the peak velocity in the bulk is calculated to be $1.7\times10^7\,cm\,s^{-1}$ at a doping concentration of $1\times10^{17}\,cm^{-3}$.

Band Structure of AlN

The high-bandgap energy of AlN of 6.2 eV at room temperature allows the bandgap in $Al_xGa_{1-x}N$ to be modified in a broad range from the value of GaN to that of AlN. With the bandgap of InN found to be even smaller than that of GaN, an even wider range is available for the material $In_xAl_{1-x}N$. Early calculations of the band structure of wurtzite and zincblende AlN are collected in [2.236]. The band structure of wurtzite AlN is calculated in [2.128]. Electronic band structure properties of zincblende AlN are further calculated by the empirical pseudopotential method in [2.108]. From these calculations, effective electron and hole mass parameters can be obtained, as compiled in Table 2.9. The direct recombination parameter is depicted in Table 2.13, taken from [2.489] and used for the development of light-emitting diodes with very high bandgap and resulting photon energy.

Indium Nitride (InN)

InN and its compounds $In_xGa_{1-x}N$ and $In_xAl_{1-x}N$ so far are not yet widely used in electronic devices [2.230]. When used, both InAlN/GaN [2.143] as well as AlGaN/InGaN [2.425] heterostructures have been reported. The indium contents are low, e.g., in [2.85, 2.150], to achieve the lattice match to GaN buffer layers. The MOCVD growth of InN is complicated caused by the high-growth temperature and resulting defect background concentrations and the high amount of residual nitrogen vacancies due to the higher growth temperatures required relative to MBE growth, as described in Chapter 3. The MBE growth of InN is under development and allows improved material quality and thus the use of the full range of material composition in the

material $In_xGa_{1-x}N$. High-quality InN has been recently grown by MBE, e.g., [2.114,2.501]. A full review of the epitaxial growth is given in [2.38]. A bulk electron mobility of 3,570 $cm^2\,V^{-1}\,s^{-1}$ at 300 K is obtained. The mobility at 150 K is as high as 5,100 $cm^2\,V^{-1}\,s^{-1}$. P-type InN has been recently reported in [2.170], which is essential for the realization of bipolar or optoelectronic pn-devices.

Mechanical and Optical Properties

An initial compilation of mechanical, optical, and thermal properties of InN is given in [2.449, 2.451]. Mechanical data are compiled in Tables 2.1 and 2.2; however, the data are relatively uncertain, due to the lack of real bulk InN material [2.449]. Elastic constants of InN are given in Table 2.3. The thermal expansion coefficients CTE in both wurtzite and zincblende structures are compiled in Table 2.5. The CTE and the lattice constants suggest the growth on sapphire substrates [2.54]. The thermal conductivity and the heat capacity of InN are still primarily based on estimates and extrapolations, as explained in [2.449], see also Table 2.16. The optical functions of InN are compiled in [2.299]. Due to the new research on samples with improved material quality, the bandgap and optical functions of InN are reconsidered, e.g., in [2.278, 2.279,2.425]. This fact also had a drastic impact on the calculation of transport properties and the higher band, which have not yet been fully repeated based on the new band structure.

Basic Carrier Transport Properties

An early compilation of the transport properties in InN is given in [2.54,2.453]. The early data are characterized by high background concentrations of 10^{19}–$10^{20}\,cm^{-3}$ and associated low mobilities. An early evaluation of the InN mobility as a function of temperature and compensation ratio using variational principle calculations is given in [2.64]. In theory, very high mobility values of 4,400 $cm^2\,V^{-1}\,s^{-1}$ are calculated, which, however, have not been fully reached experimentally. An electron mobility of 1,200 $cm^2\,V^{-1}\,s^{-1}$ and a sheet carrier concentration of $1.2 \times 10^{14}\,cm^{-2}$ have been obtained experimentally at the InN/AlN interface, as reported in [2.307]. Polarization engineering of n-InAlN/GaN HFETs and the effect on DC- and RF-performance are described in [2.186, 2.187]. The use of $In_xAl_{1-x}N$/GaN is critical, as the polarization-induced charge (PIC) is a much stronger function of the material composition x than in the AlGaN/GaN material system, as explained later. P-channel $In_xGa_{1-x}N$ HFETs based on polarization doping are demonstrated in [2.450]. Hall measurements indicate a 2D-hole gas (2DHG) mobility of approximately 700 $cm^2\,V^{-1}\,s^{-1}$ at a low temperature $T_L = 66$ K.

High-Field Transport

Mostly, the simulated results on transport in InN are still based on the assumption of a direct bandgap of InN of 1.89 eV and an associated band structure.

This was recently corrected to the much smaller bandgap value of ≈0.77 eV at room temperature [2.501]. Most of the initial MC simulations thus have to be taken with a grain of salt. Electron transport in wurtzite–InN is calculated by Leary in [2.348]. Further ensemble MC calculations on the wurtzite material by Bellotti et al. are given in [2.35]. The intervalley separation energies are given in Table 2.11. As depicted in Table 2.8, the velocity-field characteristics yield a maximum carrier velocity of up to $4.2 \times 10^7\,\mathrm{cm\,s^{-1}}$ at a critical field of about 52–65 $\mathrm{kV\,cm^{-1}}$ in the homogenous bulk case [2.113, 2.121]. These properties are promising, however, compared to GaAs or InGaAs material they are not really surprising when considering the low effective mass, the low bandgap, and maximum electron velocity. Transient-transport calculations in InN given in [2.121] report velocity overshoot values above $10^8\,\mathrm{cm\,s^{-1}}$. Quite outstanding theoretical HFET cut-off frequencies are derived from these simulations as upper bounds for a theoretical pure InN-channel-FET performance.

Band Structure

The data for the band structure of InN are taken, e.g., from the band structure calculations in [2.128], which do not yet account for the recent modification of InN bandgap energy. More experimental data on the electronic structure of MBE-grown InN are provided in [2.307]. The effective electron mass of InN has been found to be $0.11\,m_e$ [2.486], as compiled in Table 2.9. This effective mass value has to be considered high relative to the bandgap of 0.77 eV, when we compare it to other semiconductors, such as InAs or InP. Initial values of the optical bandgap of InN were reported by Tansley in [2.450]. This leads to a value of 1.89 eV at room temperature. More recent reports on the optical properties of InN, resolving the discrepancies of several publications at different growth and doping conditions, are given in [2.278, 2.279]. The bandgap of InN is found to be 0.77 eV at room temperature [2.425], as given in Table 2.10. The difference is explained by the existence of oxy-nitrides, which have a much larger bandgap. This low bandgap means a really conventional electronic III-V material, e.g., with respect to the expected breakdown of devices. Optically it means that a very broad range of wave lengths is available in the III-N systems from deep ultraviolet to red. The intervalley separation energies of both wurtzite are compiled in Table 2.11, based on the bandgap of 1.89 eV. Currently, there is little information on the intervalley energies of Zb–InN.

Boron Nitride (BN)

Boron nitride can be found in several crystallographic forms. The most important insulating or semiconducting form of BN is cubic material, which is metastable under normal conditions [2.53, 2.99, 2.253]. Ceramic BN is widely used for industrial tools as abrasive. The great advantage of cubic-BN is its Vickers hardness [2.253] and its good thermal conductivity, as compiled in Table 2.16. Even ultraviolet pn-diodes can be formed from c-BN, as given

in [2.300]. Despite the material growth problems, ultraviolet LED can be formed [2.491], which operate up to very high temperatures of 530°C [2.300].

Mechanical and Optical Properties

The mass density of cubic c-BN is given in [2.99], as compiled in Table 2.1. The outstanding Vickers hardness of BN can be observed in Table 2.2 [2.99]. Elastic constants of cubic BN are compiled in Table 2.3. The thermal expansion for cubic BN is given in Table 2.5. The values for the cubic phase are very similar to those of Zb–GaN. Thermal conductivity measurements and heat capacity measurements of cubic BN will be given in Table 2.16. The thermal conductivity of BN amounts to values of up to $750\,\mathrm{W\,m^{-1}K^{-1}}$, which is higher than in any other semiconductor. The theoretical limit found is as high as $1{,}300\,\mathrm{W\,m^{-1}K^{-1}}$.

Basic Carrier Transport Properties

Basic mobility evaluation of cubic BN as a function of carrier concentration have been provided, e.g., in [2.253]. Cubic BN is typically p-doped [2.135]. A Hall mobility of $500\,\mathrm{cm^2\,V^{-1}\,s^{-1}}$ is found at a carrier concentration of $5 \times 10^{18}\,\mathrm{cm^{-3}}$ [2.253]. For n-type material, only few experimental data exist, e.g., [2.300, 2.496]. As c-BN is an insulator [2.496], the transport is characterized by high-activation energies of the carriers of $\geq$0.2 eV.

High-Field Transport

Band structure calculations are given in [2.71] with the result that cubic BN is an insulator with a bandgap of 7.1 eV. Thus, no MC transport calculations are available for c-BN.

Dielectric Breakdown Fields

Table 2.14 compiles measured dielectric electric breakdown fields for various III-N bulk materials. The dielectric breakdown field of GaN is reported to be about $3\,\mathrm{MV\,cm^{-1}}$. AlN has a much higher breakdown field due to the higher bandgap, which can be even higher than the value given in Table 2.14 [2.388]. The dielectric breakdown field of InN is not well investigated. The latter is due to the high trap concentrations N_T and the new findings for the fundamental bandgap. The breakdown fields of bulk c-BN reported in [2.53] vary from 2 to $6\,\mathrm{MV\,cm^{-1}}$.

Table 2.14. Comparison of the bulk breakdown fields in various bulk materials at 300 K

	GaN (Wz)	Ref.	AlN (Wz)	Ref.	InN (Wz)	Ref.	BN (c)	Ref.
E_break ($\mathrm{MV\,cm^{-1}}$)	3.3	[2.61]	8.4	[2.388]	1.2	[2.244]	2–6	[2.253]

Wz wurtzite, *c* cubic

Band Structure of BN

Band structure calculations of cubic BN are available [2.496]. Similar calculations, but not of cubic phase BN, are provided in [2.237]. The bandgap of cubic BN is found to be similar to AlN and reported to be $E_g \approx 6.4\,\mathrm{eV}$ at RT in [2.253]. Further calculations of cubic BN in pseudopotential local density formalism are provided in [2.497]. The calculated charge density of the BN is very similar to other III-V semiconductors. A defect analysis of Be, Mg, and Si in cubic BN is reported in [2.135, 2.448]. The substitution of B by Mg or Be typically leads to the p-type behavior of the grown material.

2.1.2 Material Limitations

The transport properties of III-N materials and the limitations of these materials have been discussed above. Further issues are discussed in the next paragraphs.

Recombination, Generation, and Breakdown

Recombination and generation are of fundamental importance for optoelectronic and bipolar electronic devices. However, due to the influence of electron trapping in FETs, these effects also critically determine their device performance. For high-field effects at increased driving forces, an experimental evaluation of impact ionization in GaN is discussed in [2.229]. The impact ionization parameters are extracted from a AlGaN/GaN HFET device with a gate length of $0.9\,\mu\mathrm{m}$. For the high-field region of $\geq 10^6\,\mathrm{V\,cm^{-1}}$ the data can be fitted to the classical relation:

$$\alpha_n = A \cdot \exp(-K/E), \tag{2.1}$$

$$\alpha_n = 2.9 \times 10^8 \exp(-3.4 \times 10^7/E). \tag{2.2}$$

For lower fields, this expression needs to be modified, as the field dependence is weaker due to the weakness of real carrier multiplication. The relations in (2.1)/(2.2) suggest that the critical field is a factor of 8 higher when compared to GaAs-data taken from a similar extraction procedure. MC simulations of electron impact ionization in both zincblende and wurtzite GaN are provided in [2.212]. At comparable fields, the electrons are cooler in the wurtzite structure, thus the ionization rates are lower than in the zincblende phase. A similar study on the electron initiated impact ionization in Zb–GaN can be found in [2.340]. The simulations suggest a very soft breakdown threshold similar to the device findings in [2.229]. MC simulations of hole-initiated impact ionization in both GaN-phases are discussed in [2.339]. The critical field for the hole-initiated II in Zb–GaN are found to be similar to those for the electron-initiated II and amount to $3\,\mathrm{MV\,cm^{-1}}$. For the wurtzite structure, the breakdown is similar for high-electric fields, while for lower field, the hole II-rate appears to be greater. Electron-initiated impact ionization

Table 2.15. Breakdown fields, bandgap energies, and dielectric constants for various semiconductor materials

Material	Breakdown field ($\mathrm{MV\,cm^{-1}}$)	E_g (eV)	ε_r (–)	Ref.
Si	0.3	1.12	11.9	[2.463]
GaAs	0.4	1.43	12.5	[2.463]
InP	0.45	1.34	12.4	[2.463]
GaN (Wz)	3.3	3.43	9.5	[2.463]
AlN (Wz)	8.4	6.2	8.5	[2.388, 2.463]
InN (Wz)	1.2	0.7	15.3	[2.244, 2.451]
BN (c)	2–6	6.4	7.1	[2.253]
4H–SiC	3.5	3.2	10	[2.463]
6H–SiC	3.8	2.86	10	[2.463]
Diamond	5	5.6	5.5	[2.463]

in $\mathrm{Al}_x\mathrm{Ga}_{1-x}\mathrm{N}$ is evaluated by ensemble MC simulation in [2.56] for the full material composition range. The results obey the simple expression, as given in (2.1). As expected, the critical fields increase with the increase in the material composition and bandgap. Very low impact ionization rates are observed for $\mathrm{Al}_x\mathrm{Ga}_{1-x}\mathrm{N}$ in general. A study of RF-breakdown in bulk GaN and GaN MESFETs is given in [2.112]. It is found that the RF-breakdown voltage increases with the frequency of the applied RF-large-signal excitation. The difference is explained by the time-response of the particle energy. The critical field for impact ionization at AlGaN/GaN HFETs is found to be around $3\,\mathrm{MV\,cm^{-1}}$ at room temperature, as reported in [2.95]. This agrees well with the breakdown field in bulk GaN. Breakdown fields and related material properties are again compiled for comparison in Table 2.15 for various homogeneous materials. Generally, the increase of the breakdown fields with increasing bandgap is observed. The wide bandgap materials have breakdown fields, which are an order of magnitude higher than those of conventional semiconductors. The substrate material SiC and diamond have breakdown fields similar to III-N semiconductors.

2.1.3 Thermal Properties and Limitations

In addition to their electrical limits III-N semiconductor devices are subject to strong thermal (self-)heating. Table 2.16 compiles the thermal properties of several binary semiconductor materials. The temperature dependence of the thermal conductivity is modelled according to:

$$\kappa_\mathrm{L}(T_\mathrm{L}) = \kappa_{300\,\mathrm{K}} \cdot \left(\frac{T_\mathrm{L}}{300\,\mathrm{K}}\right)^{\alpha}, \tag{2.3}$$

as also stated in Chapter 8.

Table 2.16. Thermal properties of III-nitride binary and ternary materials at 300 K

	κ_{300} ($\mathrm{W\,K^{-1}\,m^{-1}}$)	α (–)	c_{300} ($\mathrm{J\,K^{-1}\,kg^{-1}}$)	Ref.
Si	148	−1.35	711	[2.406]
GaAs	54	−1.25	322	[2.356]
InP	68	−1.4	410	[2.356]
GaN (Wz)	130	−0.43	491	[2.120, 2.423]
AlN (Wz)	285	−1.57	748	[2.428]
InN (Wz)	38.5, 45, 80,176	–	325	[2.223, 2.428, 2.449]
BN (c)	749	–	600	[2.99]
6H–SiC	390	−1.5	715	[2.57]
6H–SiC	490	–	690	[2.244, 2.331]
4H–SiC	330	–	690	[2.244, 2.416]
V-doped SiC	370	–	690	–
Sapphire	42	–	750	–
Diamond	2,000–2,500	−1.85	520	[2.405]

Thermal Conductivity and Heat Capacity

Silicon serves as a reference. The thermal conductivity of silicon is not reached by GaAs. On the contrary, GaN has a thermal conductivity similar to silicon. The thermal conductivity at 300 K κ_{300} of AlN is better than the κ_{300} of GaN, while InN has a very low value [2.223]. BN has the best value of all III-N materials. Initial determination of thermal properties of GaN is given in [2.423]. Further thermal data is compiled in [2.4]. The intrinsic thermal conductivity for AlN is determined in [2.428]. The thermal conductivity of GaN is often quoted dating back to the work of Sichel [2.423]. However, several investigations are available which especially focus on the effects of dislocations on the thermal conductivity. A good overview of the data are presented and the methods of measurements are compiled in [2.120]. The effect of dislocations on the thermal conductivity in GaN is investigated experimentally in [2.264]. The measurements show a dramatic increase of the thermal conductivity at reduced dislocation density of $10^8\,\mathrm{cm^{-2}}$, especially at temperatures below 200 K. The theoretical predictions in [2.216] support a maximum value for the thermal conductivity in GaN of nearly $200\,\mathrm{W\,K^{-1}\,m^{-1}}$. The experimental data for the thermal conductivity of InN ($\leq 45\,\mathrm{W\,K^{-1}\,m^{-1}}$) is much lower than the theoretical predictions of $176\,\mathrm{W\,K^{-1}\,m^{-1}}$ [2.223].

The data for the heat capacity are also compiled in Table 2.16. The heat capacity is given for constant pressure. For SiC, the measured value of the polytype 6H–SiC is used for SiC in general [2.356]. The heat capacity of the binary semiconductors is lower than of the substrate material. More analysis with respect to the packaging materials and to the dynamic response is provided in Chapter 8.

2.1.4 Ternary and Quaternary III-N Materials

The existence of ternary and even quaternary materials in the III-N system is a fundamental advantage relative to other wide bandgap semiconductor materials, such as SiC. The possibility of growing $Al_xGa_{1-x}N$, $In_xGa_{1-x}N$, and $In_xAl_{1-x}N$ in heterostructures with the III-N binaries allows bandgap engineering. This has tremendous impact on the electronic and optoelectronic application of the materials. The material parameters of the quantity P are combined by quadratic interpolation in the following two approaches:

$$P_{A_xB_{1-x}N} = P_A \cdot x + P_B \cdot (1-x) + C_{P,AB} \cdot x \cdot (1-x). \tag{2.4}$$

In the second approach, (2.4) can be written in another way, i.e.:

$$P_{A_xB_{1-x}N} = a + b \cdot x + c \cdot x^2 \tag{2.5}$$

resulting in different coefficients, which can be directly correlated with the binary materials. Sometimes (2.5) is extended to a third-order polynomial:

$$P_{A_xB_{1-x}N} = a + b \cdot x + c \cdot x^2 + d \cdot x^3. \tag{2.6}$$

All relevant quantities will be analyzed in the following sections using the aforementioned formulae in quadratic interpolation. If necessary, cubic or other interpolation schemes will be mentioned.

Aluminum Gallium Nitride ($Al_xGa_{1-x}N$)

$Al_xGa_{1-x}N$ is the most important ternary compound, as the lattice-mismatch relative to GaN can be effectively controlled for nearly all material compositions. A distinction may be required for wurtzite and zincblende AlGaN materials, as the zincblende material has a transition from a direct to an indirect semiconductor [2.235].

Mechanical and Optical Properties

For mass density, Vickers hardness, and dielectric constants, typically no bowing is applied, and the values can be interpolated linearly with high precision between the binary values of GaN and AlN. The heat capacity of the ternaries is interpolated linearly as given in (2.7):

$$c_{L,AB} = (1-x) \cdot c_{L,A} + x \cdot c_{L,B}. \tag{2.7}$$

The thermal conductivity of $Al_xGa_{1-x}N$ is interpolated as the following equation (2.8), taken from [2.357]. Data for the thermal conductivity of $Al_xGa_{1-x}N$ is given in [2.255]. The derived parameters are given in Table 2.17.

$$\kappa_{AB} = \left(\frac{(1-x)}{\kappa_A} + \frac{x}{\kappa_B} + \frac{x \cdot (1-x)}{C_{\kappa,AB}} \right)^{-1}. \tag{2.8}$$